Astronomy & Astrophysics manuscript no. aa62069-261
October 30, 2026
©ESO 2026

Height-dependent thermal properties of extreme-ultraviolet campfires in the quiet Sun

O. Podladchikova[1,2,⋆], A. Warmuth[1], L. Harra[2,3], C. Verbeeck[4], M. K. Georgoulis[5,6], A. M. Veronig[7,8], D. Müller[9], S. J. Hofmeister[10,1], P. Antolin[11], M. Haberreiter[2], S. Purkhart[7], D. M. Long[12], A. F. Battaglia[13], N. Engler[2,3], É. Buchlin[15], L. Dolla[4], M. Mierla[4,14], L. Rodriguez[4], M. J. West[9], A. N. Zhukov[4], E. Soubrié[15,16], V. Büchel[2], A. De Groof[17], M. Gyo[2], J. P. Halain[9,18], B. Inhester[19], E. Kraaikamp[4], D. Pfiffner[2], P. Rochus[†18,⋆⋆], F. Schuller[1], P. J. Smith[20], W. Schmutz[2], and K. Stegen[4]

(Affiliations can be found after the references)

Received ...; accepted...

ABSTRACT

Context. Small-scale impulsive energy-release events are widely considered a key ingredient of quiet-Sun coronal heating. The discovery of extreme ultraviolet (EUV) campfires by Solar Orbiter has opened a new observational window at unprecedented spatial scales.

Aims. We quantified the thermal-energy content of EUV campfires, examined their impulsive heating characteristics, and investigated how their properties vary with atmospheric height.

Methods. We analysed the complete set of campfires obtained in a single observing sequence on 30 May 2020 with Solar Orbiter/EUI $\mathrm{HRI_{EUV}}$ at 174 Å. Temperatures and emission measures were adopted from SDO/AIA diagnostics, and geometric uncertainties were explored using multiple volume models. Statistical properties were characterised using cumulative distribution functions and maximum-likelihood techniques, and results were compared with Solar Orbiter/STIX microflares and SDO/AIA nanoflare-like events for context.

Results. Campfire durations show a clear dependence on height: short-duration events occur at all heights, whereas longer-lived brightenings are preferentially associated with chromospheric layers. Emitting volumes and thermal energies, by contrast, show no comparable height dependence. The background-subtracted thermal energies span $\sim 10^{20}$–10^{24} erg, with rare events reaching $\sim 5 \times 10^{24}$ erg. The statistically robust power-law regime extends over $\sim 10^{22}$–10^{24} erg, while non-background-subtracted estimates are systematically higher by approximately one order of magnitude. Directly detected campfires contribute a sub-percent fraction of the canonical quiet-Sun heating requirement. Accounting approximately for the detection threshold and differential emission measure completeness could raise this contribution to a value of order a few percent, though this remains a single-epoch, order-of-magnitude estimate.

Conclusions. Extreme ultraviolet campfires extend the flare energy distribution towards lower energies and provide height-resolved constraints on impulsive heating in the quiet Sun. The height dependence of event durations – driven mainly by an excess of long-lived events in the lower chromosphere – combined with broadly invariant energy and volume distributions, indicates that atmospheric stratification primarily modulates cooling and dissipation timescales rather than the characteristic energy scale of the heating process.

Key words. Sun: activity – Sun: chromosphere – Sun: corona – Sun: flares – Sun: UV radiation – Sun: X-rays, gamma rays

arXiv:2510.10340v6 [astro-ph.SR] 27 Oct 2026

1. Introduction

Understanding the mechanisms responsible for heating the solar corona remains one of the central open questions of solar physics. Maintaining coronal temperatures requires a continuous energy input from the solar magnetic field, yet the physical processes by which this energy is transported and dissipated remain debated. Both observations and theory indicate that coronal heating is fundamentally impulsive, with energy released through numerous small-scale events – driven by magnetic reconnection, turbulent wave dissipation, or both – rather than as a steady process.

Coronal heating is now understood as a multi-scale problem involving the generation, transport, and dissipation of magnetic energy across a broad range of spatial and temporal scales. Two broad paradigms have traditionally been invoked: wave-based heating and impulsive (nanoflare-like) heating. While often treated as distinct, these processes represent complementary manifestations of the same underlying physics – the conversion of magnetic energy into plasma heating through electric currents and electromagnetic stresses (Benz 2008; Klimchuk 2015). Photospheric motions inevitably stress coronal magnetic fields, generating currents throughout the atmosphere that dissipate either directly or through wave–particle interactions, depending on plasma conditions and magnetic topology.

A useful physical distinction can be drawn between dissipation driven by currents perpendicular to the magnetic field and those aligned parallel to it (Spicer & Brown 1980; Priest & Forbes 2000). Perpendicular currents drive magnetic reconnection on Alfvénic timescales through extremely thin current sheets, whereas field-aligned current dissipation proceeds through anomalous resistivity and current-driven instabilities, converting magnetic energy more directly into heat. In both cases, energy release occurs in collisionless plasma through wave–particle interactions (Leontovich 1975). In the low corona and upper transition region, where plasma-β approaches unity, quasi-parallel current sheets are expected to be systematically wider than those forming higher in the corona, favouring gentler, thermally dominated energy release (Demoulin & Klein 2000).

⋆ Corresponding author: O. Podladchikova, e-mail: epodlad@gmail.com
⋆⋆ In memoriam

Wave heating and impulsive heating should therefore be viewed not as competing mechanisms but as limiting cases of magnetic-energy dissipation operating on different scales. Wave dissipation is particularly effective in long coronal loops and open magnetic structures, where Alfvén waves cascade to small scales via turbulence (Heyvaerts & Priest 1983). Observational evidence shows that Alfvénic waves also dissipate at low coronal heights, contributing to the heating of short loops and quiet-Sun regions (e.g. Tomczyk et al. 2007; Hahn & Savin 2014; Hahn et al. 2025). The two scenarios have a common requirement: magnetic energy injected at large scales must cascade efficiently to the small scales where dissipation occurs.

Extreme-ultraviolet (EUV) and X-ray diagnostics measure macroscopic plasma properties – temperature and emission measure – that represent statistical averages over many unresolved dissipation sites. As noted by Benz (2008), these thermodynamic quantities are fully consistent with kinetic descriptions of energy release even without direct evidence of non-thermal particles. Magnetohydrodynamic (MHD) descriptions capture the large-scale plasma response, while the actual energy conversion occurs at much smaller, often unresolvable scales.

A broad theoretical consensus holds that the corona is heated by a hierarchy of impulsive events that span a wide energy range. The nanoflare hypothesis (Parker 1988) formalised this picture, and subsequent simulations and statistical studies have shown that such heating naturally produces scale-free energy distributions and intermittent plasma response (e.g. Vlahos et al. 1995; Georgoulis et al. 1998; Rappazzo et al. 2008; Guerreiro et al. 2017). Klimchuk (2015, 2017) emphasised that nanoflares are expected to remain below direct observational resolution, with EUV and X-ray observations capturing only their macroscopic thermal signatures. Wave-heating models – particularly those involving counter-propagating Alfvén waves – remain equally viable and have received strong observational support (e.g. Tomczyk et al. 2007; Hahn & Savin 2014; De Moortel & Browning 2015; Cranmer et al. 2017; Hahn et al. 2025). The two paradigms are not mutually exclusive and may operate together or in different regions.

Recent instrumental advances have begun to probe this regime directly. High-resolution EUV imagers such as Hi-C (Subramanian et al. 2018) and the Extreme Ultraviolet Imager (EUI) aboard Solar Orbiter (Müller et al. 2020; Rochus et al. 2020) have revealed abundant small-scale brightenings in the quiet Sun. The discovery of 'EUV campfires' by Berghmans et al. (2021) demonstrated that impulsive heating events occur ubiquitously in the low corona at energies well below those of classical nanoflares. Subsequent observations have extended this picture to previously unexplored spatial and temporal scales (Chitta et al. 2023, 2025) and to less accessible low coronal layers (Chitta et al. 2021).

Crucially, this progress does not imply that elementary dissipation scales are being resolved. Rather, it constrains the macroscopic plasma response – thermal energy content, characteristic timescales, spatial extent, and height distribution – associated with impulsive heating, precisely the regime predicted by nanoflare theory to be observationally accessible (Klimchuk 2015, 2017). In this work, we analysed EUV campfires from the Solar Orbiter/EUI catalogue of Berghmans et al. (2021). We performed a systematic analysis of their thermodynamic properties, thermal energies, and statistical distributions, assessing robustness against geometric assumptions. For context, we compared the campfire population with microflares observed by the Spectrometer/Telescope for Imaging X-rays (STIX) on Solar Orbiter (Battaglia et al. 2021) and with nanoflare-like events observed by the Atmospheric Imaging Assembly (AIA) on the Solar Dynamics Observatory (SDO) (Purkhart & Veronig 2022). A key aspect of this study is the layer-resolved characterisation of campfire properties across atmospheric layers, which provides new constraints on how dissipation timescales vary with plasma conditions. We emphasise that our analysis constrains observable thermal envelopes rather than the microscopic dissipation sites themselves.

2. Observations and data analysis

2.1. Observational setup and dataset

This study uses the observations obtained on 30 May 2020 by the High-Resolution Imager in the extreme ultraviolet (HRI_{EUV}) of the EUI aboard Solar Orbiter (Müller et al. 2020). At the time of observation, Solar Orbiter was at a heliocentric distance of 0.556 au. With its plate scale of $0.49''$ pixel^{-1}, compared with $0.6''$ pixel^{-1} for the SDO/AIA (Lemen et al. 2012), and owing to the reduced solar distance, HRI_{EUV} resolves a projected pixel scale of ≈198 km at the solar surface, about 2.2 times finer than the ≈435 km of AIA at 1 au.

HRI_{EUV} observes in a narrow passband centred at 174 Å, dominated by Fe IX/Fe X emission and sensitive to plasma near 1 MK, characteristic of the quiet-Sun corona. The effective pixel scale at the solar surface was 198 km, with a temporal cadence of 5 s per frame, sufficient to resolve the rapid evolution of transient brightenings.

We analysed EUV campfires from the catalogue of Berghmans et al. (2021). The image sequence spans 245 s over a field of view of approximately $17' \times 17'$ ($\sim 1.7 \times 10^{21}$ cm^2, or $\approx 411 \times 411$ Mm^2). The observations were obtained near solar minimum, with no active regions in the field of view, making the dataset well suited for studying weak, small-scale energy-release events free from active-region contamination.

All data were calibrated using the standard EUI pipeline described in Berghmans et al. (2021) (hereafter Paper I), including corrections for dark current, flat-field, detector degradation, and pointing. No additional processing was applied beyond what was presented in Paper I.

2.2. Campfire event sample and co-identification

The campfire sample is drawn from the event catalogue of Berghmans et al. (2021). We used the primary sample of 1,468 campfires detected at $\geq 5\sigma$.

All events were co-identified in simultaneous SDO (Pesnell et al. 2012) AIA 171 Å and 193 Å observations (Lemen et al. 2012), from which thermodynamic parameters (temperature and emission measure) were derived in Paper I using differential emission measure (DEM) analysis. The same co-identification enabled subsequent stereoscopic height determinations in Paper II (Zhukov et al. 2021). Throughout this paper, 'EUV campfires' refers exclusively to the events catalogued by Berghmans et al. (2021). Figure 1 shows representative campfire events, illustrating their morphology, segmentation, and the geometric parameters used in this study.

2.3. Event definition and geometric characterisation

Event identification, tracking, and lifetime determination follow the definitions of Paper I. An event is a spatially connected set of pixels persisting over consecutive frames, with its lifetime measured between the first and last frames exceeding the detection

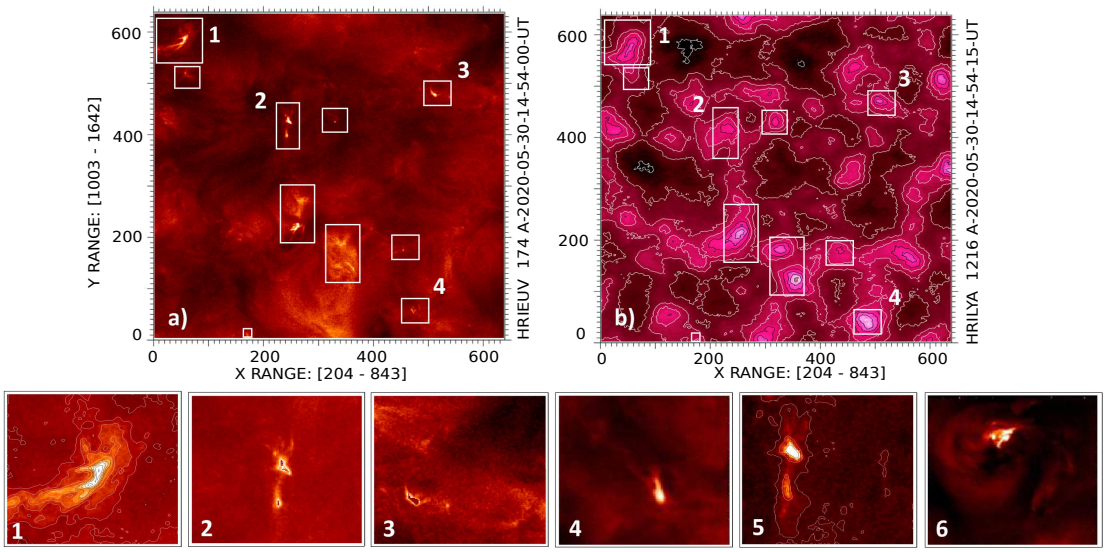

Fig. 1. Representative EUV campfires from the Solar Orbiter $\mathrm{HRI_{EUV}}$ catalogue of Berghmans et al. (2021), observed at 174 Å on 30 May 2020. *Panel (a)*: $\mathrm{HRI_{EUV}}$ 174 Å field of view with campfire locations marked. *Panel (b)*: Co-temporal $\mathrm{HRI_{Lya}}$ 1216 Å image with Lyα network contours. *Bottom row*: Events 1–6. Events 1–4 lie above the Lyα network and are marked in panels (a) and (b). Events 5 and 6 originate from other quiet-Sun regions. The bottom row illustrates a range of morphologies, including compact brightenings, loop-like structures, and events with apparent flows. Animations corresponding to panels (a) and (b) and events 1–6 are available online.

threshold; the minimum detectable duration corresponds to a single 5 s frame. Energetics are characterised using the peak values of emission measure and temperature reached over the event lifetime rather than integrated over the full duration. At this stage, the spatial extent is quantified using geometrical descriptors derived from the intensity distribution: the projected area, the major axis (L) and minor axis (W) from second moments, and the bounding-box dimensions.

3. Thermal energy framework

3.1. Thermal energy formulation

We focused exclusively on the thermal component of the energy budget inferred from EUV observations, combining thermodynamic diagnostics with geometrical source characterisation and explicit background subtraction. For an optically thin coronal plasma, the thermal energy of a heating event is

$$E_{\mathrm{th}} = 3\, k_{\mathrm{B}}\, T\, n_{\mathrm{e}}\, V,$$

where k_{B} is the Boltzmann constant, T the plasma temperature, n_{e} the electron number density, and V the emitting volume. For a fully ionised hydrogen plasma, $n_{\mathrm{tot}} \approx 2\, n_{\mathrm{e}}$, and the factor 3 accounts for both electrons and ions (Aschwanden et al. 2000).

Since n_{e} is not directly observable, we express the thermal energy in terms of the emission measure. DEM analysis yields the column emission measure,

$$\mathrm{EM_{col}} = \int n_{\mathrm{e}}^2 \, \mathrm{d}s,$$

integrated along the line of sight. Given an effective emitting depth h_{eff} and projected source area A, the volume emission measure is

$$\mathrm{EM_{vol}} = \mathrm{EM_{col}}\, A,$$

and the thermal energy becomes

$$E_{\mathrm{th}} = 3\, k_{\mathrm{B}}\, T\, A\, \sqrt{\mathrm{EM_{col}}\, h_{\mathrm{eff}}} = 3\, k_{\mathrm{B}}\, T\, \sqrt{\mathrm{EM_{vol}}\, V},$$

which follows from $\mathrm{EM_{vol}} = n_{\mathrm{e}}^2\, V$ and $E_{\mathrm{th}} = 3\, n_{\mathrm{e}}\, k_{\mathrm{B}}\, T\, V$. For the reference energy estimates, we adopted $EM_{\mathrm{vol}} = EM_{\mathrm{col}} A_{\mathrm{proj}}$ with the baseline effective volume V_{proj} defined in Sect. 3.4.

In practice, E_{th} was computed from background-subtracted peak values of emission measure and temperature – EM_{max} and T_{max} – evaluated at the single time step of maximum spatially integrated EUV intensity. This instantaneous estimate is combined with the emitting volume at the same time step, and is fully equivalent to using the volume emission measure directly. It enables comparisons with previous EUV and X-ray studies (Aschwanden et al. 2000; Ulyanov et al. 2019) and forms the basis for all subsequent energy estimates. As the plasma undergoes ongoing radiative and conductive losses throughout the event lifetime, this peak thermal energy represents a conservative estimate of the total heating requirement; radiative losses are addressed quantitatively in Sect. 4.4. Geometric volume assumptions are explored in Sect. 3.4.

3.2. Thermodynamic parameters and background subtraction

Temperatures and column emission measures were adopted from Paper I, where they were derived via DEM analysis using the regularised inversion code of Hannah & Kontar (2012) applied to co-temporal SDO/AIA multi-channel observations and validated through cross-channel consistency checks. The Spectral Imaging of the Coronal Environment (SPICE) instrument aboard Solar Orbiter was not yet operational on 30 May 2020, making SDO/AIA the only available multi-temperature diagnostic. Re-analyses using AIA time-lag techniques (Dolliou et al. 2023) and SPICE observations of similar events (Dolliou et al. 2024; Huang et al. 2023) are discussed in Sect. 4.5.

In the quiet Sun, a substantial fraction of the observed EUV emission originates from pre-existing coronal plasma unrelated to the impulsive event. To isolate the transient thermal signature, we computed both raw and background-subtracted thermodynamic parameters. For each campfire, the DEM was obtained using the regularised inversion method of Hannah & Kontar (2012)

applied to the 5σ detections. For the background-subtracted data, the background immediately preceding each event was estimated using the inpainting method of Bertalmío et al. (2001), which estimates the intensity and intensity gradient within the masked region to match the surrounding boundary, and removed prior to the DEM inversion. Background-subtracted values represent the excess thermal plasma produced by the impulsive episode; non-subtracted values reflect the total emitting structure along the line of sight. Unless stated otherwise, background-subtracted parameters were used for all energy estimates, consistent with standard practice in flare and nanoflare studies. Of the 1,468 campfires, 558 have valid DEM solutions without background subtraction, and 389 retain robust solutions after background subtraction; only these 389 events (~26% of the sample) were included in the energy analysis.

Throughout this work, the height of each event refers to its stereoscopic altitude above the solar surface, determined in Paper II (Zhukov et al. 2021) from the simultaneous SDO and Solar Orbiter vantage points. Events were grouped into atmospheric layers according to this stereoscopic height, following Judge (2006) (see our Table 1). This geometric height gives the vertical position of the event in the atmosphere and is distinct from the effective emitting depth ($h_{\rm eff}$) along the line of sight, introduced earlier in the thermal energy formulation. The effective depth $h_{\rm eff}$ and volume V cannot be measured directly and are constrained via the geometrical models introduced in Sect. 3.4.

The fraction of events retaining a robust DEM solution shows no systematic trend with height (ranging from ~22% to ~39% across layers, without a monotonic dependence), confirming that the DEM-based subsample is not preferentially biased towards any particular atmospheric layer. The height-resolved comparison of thermal properties is therefore unaffected by DEM completeness. The subsample is, however, biased towards larger and longer-lived events, for which the emission-measure signal is sufficient for a stable inversion; energy-based conclusions accordingly refer to this brighter population. We stress that the duration–height relation itself is derived from the full sample of 1,468 events, for which durations and heights are available independently of the DEM inversion, and is therefore not affected by this selection. The thermal-energy comparison across layers, by contrast, uses the 389-event subsample; within this subsample the energies show at most a weak dependence on height, much smaller than the variation in duration measured on the full sample.

3.3. Thermodynamic properties and *EM–T* scaling

The emission measure–temperature (*EM–T*) plane provides a compact characterisation of the thermal plasma response to impulsive energy release. Temperature describes how strongly the emitting plasma is heated, whereas the emission measure quantifies the amount of plasma contributing to the observed emission. In X-ray flare studies these quantities are routinely derived from spectral or broadband measurements and used to compare the thermal properties of events over a wide range of magnitudes (e.g. Aschwanden 2004; Warmuth & Mann 2016). Here, the DEM analysis of the co-temporal SDO/AIA observations allows EUV campfires to be placed in the same thermodynamic parameter space, testing whether they extend the empirical *EM–T* scaling of nanoflares and larger flares towards lower temperatures and emission measures (e.g. Joulin et al. 2016; Purkhart & Veronig 2022). The comparison concerns the thermal plasma response only and does not constrain a non-thermal particle component.

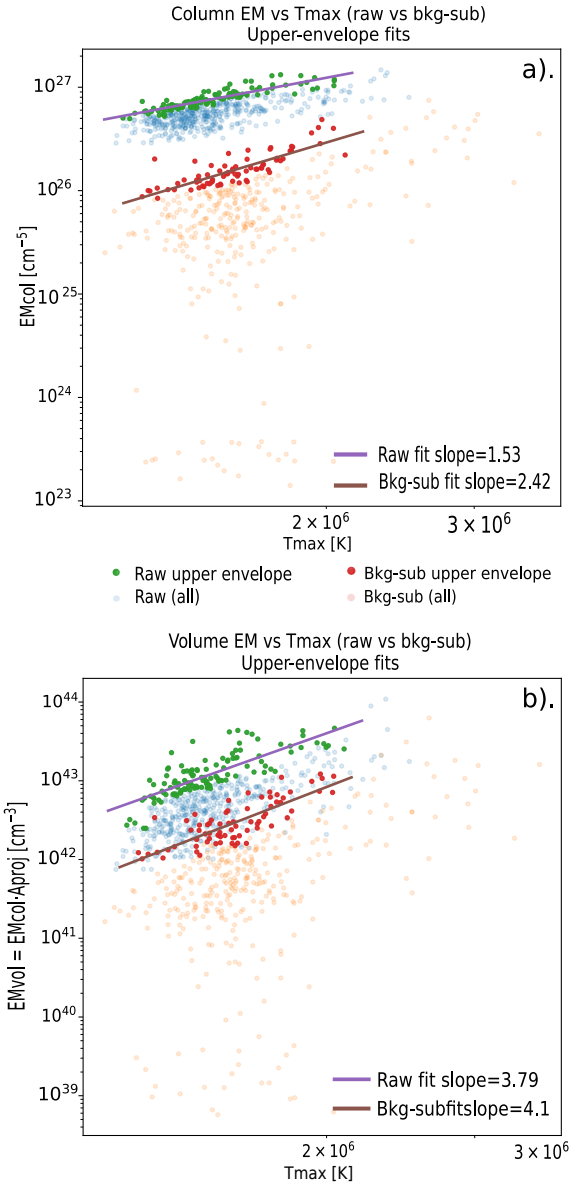

Fig. 2. Emission measure–temperature (*EM–T*) relations for campfires. *Top*: Column emission measure ($EM_{\rm col}$) versus temperature. *Bottom*: Volume emission measure, $EM_{\rm vol} = EM_{\rm col}\,A_{\rm proj}$. Blue and orange points show all events without and with background subtraction, respectively. Green and red filled circles mark the upper-envelope points; purple and brown lines show power-law fits to the raw and background-subtracted upper envelopes, with slopes indicated. The upper envelope – the locus of maximum *EM* at each temperature – is fitted rather than the full distribution because it traces the most energetic events, is less sensitive to detection incompleteness at low energies, and enables direct comparisons with published *EM–T* scaling relations (e.g. Aschwanden 2004; Warmuth & Mann 2016). The two fits shown in each panel correspond to the raw and background-subtracted upper envelopes: for $EM_{\rm col}$ the slopes are 1.53 (raw) and 2.42 (background-subtracted), and for $EM_{\rm vol}$ they are 3.79 (raw) and 4.1 (background-subtracted).

In Fig. 2, each point corresponds to a single campfire. The values used are the maximum column emission measure and the maximum DEM-weighted temperature (following the definition of Parenti et al. 2017), taken over all spatial pixels and time steps belonging to each campfire and determined independently, so that the two maxima need not occur at the same pixel or time; both are derived from the DEM maps of Paper I (Bergh-

mans et al. 2021), which employs the DEM method of Hannah & Kontar (2012). The volume emission measure follows as $EM_{\rm vol} = EM_{\rm col}\,A_{\rm proj}$. Values obtained with and without background subtraction are shown separately, and the background-subtracted values are used for all energy estimates. The upper-envelope points (green and red) trace the maximum EM reached as a function of temperature, and it is these that the power-law fits describe.

Campfires show temperatures of $T \sim$ 1–2 MK, consistent with their detection in the EUI 174 Å passband. Their emission measures span several orders of magnitude, reflecting a broad range of event energetics. Recent analyses suggest that a significant fraction of campfire plasma does not reach coronal temperatures (Dolliou et al. 2023, 2024; Huang et al. 2023); the thermal energies derived here therefore characterise only the coronal (∼1 MK) component visible in this passband.

Power-law fits to this upper envelope are overplotted in Fig. 2. For the background-subtracted data, the upper-envelope slopes are 2.42 for $EM_{\rm col}$ and 4.1 for $EM_{\rm vol}$. These values are comparable to those reported for impulsively heated coronal loops, nanoflares, and larger flares (e.g. Aschwanden 2004; Warmuth & Mann 2016); in particular, the $EM_{\rm vol} \propto T^{4.1}$ scaling is consistent with the $EM \propto T^4$ relation found for larger flares (Warmuth & Mann 2016), supporting the interpretation of campfires as the low-energy extension of impulsive heating in magnetically confined plasma.

3.4. Geometrical volume models

We considered four effective volume models spanning the range commonly used in nanoflare and EUV energetics studies, all evaluated at the time of peak emission. Models $V_{\rm proj}$, $V_{\rm cyl}$, and $V_{\rm box}$ include a filling factor of 0.1, consistent with values adopted in previous studies (Aschwanden et al. 2000; Ulyanov et al. 2019) and supported by an independent check: comparing $V_{\rm EUV}$ with $V_{\rm box}$ yields filling-factor ratios of 0.07–0.17 (mean ≈0.13). The $V_{\rm EUV}$ model intrinsically represents the EUV-emitting fraction and requires no additional filling factor.

The area–depth scaling ($V_{\rm proj}$; a scale-free proxy) is

$$V_{\rm proj} = 0.1\,A_{\rm proj}\,\sqrt{A_{\rm proj}},$$

where $A_{\rm proj}$ is the projected emitting area at peak emission. The line-of-sight depth scales with $\sqrt{A_{\rm proj}}$, yielding a scale-free estimate applicable when no specific loop geometry is assumed. This is the baseline model used throughout unless stated otherwise.

The cylindrical loop volume ($V_{\rm cyl}$) is

$$V_{\rm cyl} = 0.1\,\pi\left(\frac{W}{2}\right)^2 L,$$

where L and W are the major and minor axes from second-moment analysis. This model assumes a straight cylindrical loop with circular cross-section.

The bounding-box scaling ($V_{\rm box}$) is

$$V_{\rm box} = 0.1\,A_{\rm box}\,\sqrt{A_{\rm box}},$$

where $A_{\rm box} = L_{\rm box} W_{\rm box}$ is the minimal bounding-rectangle area. This model accommodates irregular or multi-stranded morphologies.

The Aschwanden-type elliptical-loop EUV volume ($V_{\rm EUV}$) is

$$V_{\rm EUV} = V_{\rm loop}\left[1 - \frac{2}{\pi}\arctan\left(\frac{h_{\rm ch}}{L/2}\right)\right], \qquad V_{\rm loop} = \frac{\pi^2}{4}\,r\,w^2,$$

with

$$r = \sqrt{\left(\frac{L}{2}\right)^2 + h_{\rm ch}^2} - \frac{w}{2},$$

where L and w are the ellipse major and minor axes, and $h_{\rm ch}$ is the chromospheric height below which EUV emission is suppressed. Classical nanoflare studies adopt $h_{\rm ch} \sim 2500$ km (e.g. Aschwanden et al. 2000); here we used $h_{\rm ch} = 150$ km, motivated by stereoscopic measurements that show that campfires form at exceptionally low altitudes, often well below 1 Mm (Zhukov et al. 2021). We note that $h_{\rm ch}$ is a physical opacity cutoff, not a minimum campfire height; the observed height distribution (Fig. 7) shows events typically above ∼500 km, while $h_{\rm ch}$ describes the layer below which EUV emission is suppressed regardless of event location. This model describes the EUV-bright coronal portion of a semi-circular loop (Aschwanden et al. 2000) and requires no filling factor.

3.5. Scope and limitations

The thermal energies derived here represent only the excess thermal component inferred from EUV emission, and the statistical properties of the campfire population – energy range, distribution shape, and scaling behaviour – are robust against reasonable variations in geometry and background subtraction. A quantitative assessment of geometric uncertainties is given in Sect. 4.2, and the broader limitations of the analysis are discussed in Sect. 4.6.

4. Results

We first characterised the morphology and source geometry of the campfire population, then quantified their thermal energies and statistical distributions, and finally examined how these properties vary with atmospheric height. Throughout, statistical distributions are characterised using complementary cumulative distribution functions (CCDFs) and power-law slopes estimated via maximum likelihood, which together provide robust, binning-independent diagnostics of the underlying populations.

4.1. Morphology and source geometry

Figures 3 and 4 show CCDFs of campfire morphological parameters and geometric volumes evaluated at peak emission, where the CCDF $P(X \geq x)$ gives the fraction of events with a value greater than or equal to x. Projected source areas are computed assuming an elliptical geometry defined by second-moment axes, following an Aschwanden-type formulation that avoids assumptions of cylindrical symmetry.

All geometric quantities exhibit power-law tails towards larger values, though the fitted regime spans less than one decade above $x_{\rm min}$. Slopes vary across geometric models but remain consistent within their bootstrap uncertainties – confidence intervals obtained by repeatedly resampling the data with replacement and refitting, which quantify how sensitive the slope is to the particular set of detected events. The slopes are also stable against conservative assumptions about spatial resolution, segmentation, and pointing jitter.

Power-law indices are estimated via maximum-likelihood estimation (Clauset et al. 2009; Verbeeck et al. 2019), with the lower cutoff $x_{\rm min}$ selected objectively via the Kolmogorov–Smirnov (KS) criterion (Clauset et al. 2009). This approach

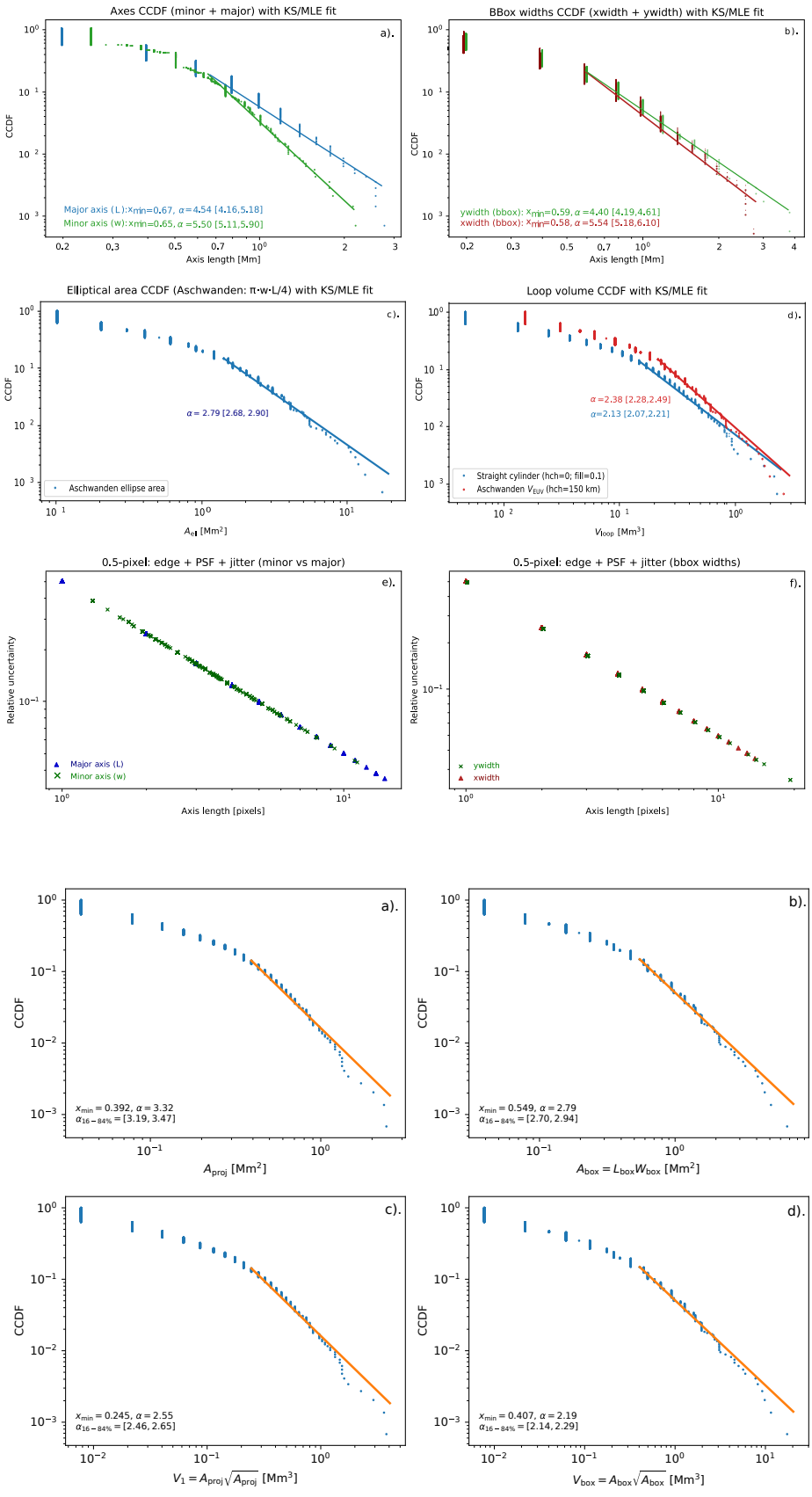

Fig. 3. CCDFs of campfire morphological and geometric parameters at peak emission. *Panel (a)*: Minor axis (W; blue) and major axis (L; green). *Panel (b)*: Bounding-box widths in the x- (red) and y-direction (green). *Panel (c)*: Elliptical projected area $A_{ell} = \pi\, W\, L/4$. *Panel (d)*: Effective loop volume for a straight-cylinder model (blue) and the Aschwanden V_{EUV} model (red). *Panels (e) and (f)*: Relative uncertainties as a function of axis length and bounding-box width in pixels under a conservative half-pixel error; in each panel the two parameters are shown with different symbols (triangles and crosses) for clarity. The concentration near ∼0.2 Mm in (a) and (b) reflects the minimum detectable size of one pixel (≈198 km). Power-law fits to the high-value tails are shown in (a)–(d), with the lower cutoff (x_{min}) from the KS criterion and indices α via maximum likelihood. Vertical bars show bootstrap confidence intervals (16th–84th percentiles).

Fig. 4. CCDFs of campfire geometric quantities: (a) projected area (A_{proj}), (b) bounding-box area ($A_{box} = L_{box}W_{box}$), (c) effective volume ($V_1 = A_{proj}\sqrt{A_{proj}}$), and (d) $V_{box} = A_{box}\sqrt{A_{box}}$. Power-law fits are shown for the high-value tails above the KS-determined cutoff, x_{min}. Slopes (α) are estimated via maximum likelihood with bootstrap confidence intervals ($\alpha_{16-84\%}$); the values are indicated in each panel.

yields unbiased slope estimates and enables direct comparisons with nanoflare and flare studies, where power-law slopes are a key diagnostic of coronal heating (Hudson 1991). We do not claim that a power law is the unique description of the data. Following Clauset et al. (2009), we first verified the power-law hypothesis itself using a bootstrap KS goodness-of-fit test (10^3

synthetic samples): the fit is not rejected ($D = 0.05$, $p = 0.60$), so a power law is a plausible description of the tail. We then compared it against alternative distributions using normalised likelihood ratios. A pure exponential is rejected ($R = 2.6$, $p = 0.008$), confirming that the distribution is genuinely heavy-tailed. A log-normal, by contrast, cannot be statistically distinguished from a power law over the limited dynamic range probed here ($p = 0.33$), consistent with the observational finding of Verbeeck et al. (2019) that solar-flare energy distributions can be equally well described by a log-normal. Such behaviour is expected in self-organised critical systems (Bak et al. 1987), where avalanche-like energy release follows a power law when events are small compared with the system size but departs towards a log-normal as the largest events approach the system scale (Vlahos et al. 1995; Georgoulis & Vlahos 1996). Crucially, the physically relevant quantity for coronal-heating arguments – the slope of the high-value tail ($\alpha \approx 2.2$) – is robust to the choice between these forms; our conclusions rest on the heavy-tailed character and tail slope of the distribution rather than on a specific functional model.

4.2. Uncertainty propagation

Geometric uncertainties arise primarily from finite spatial resolution and segmentation. We adopted a conservative total uncertainty of $\sigma_{\rm pix} = 0.5$ pixel (≈100 km) per length scale, combining contributions from edge definition, point-spread function, and pointing jitter. Although the Nyquist-limited resolution of $\mathrm{HRI_{EUV}}$ is 2 pixels (≈400 km), moment-based axes L and W are computed from intensity-weighted second moments over the full event area, reducing the effective uncertainty well below one pixel for all but the smallest events. This yields relative uncertainties of ∼1–3% for large events and ∼3–7% for typical events (see the bottom row of Fig. 3).

For volume models of the form $V \propto W^2 L$,

$$\frac{\sigma_V}{V} = \sqrt{\left(2\frac{\sigma_W}{W}\right)^2 + \left(\frac{\sigma_L}{L}\right)^2}.$$

Since $E_{\rm th} \propto \sqrt{V}$ (from $E_{\rm th} = 3\,k_{\rm B}\,T\,n_e\,V$ and $n_e \propto \sqrt{\mathrm{EM_{vol}}/V}$), thermal-energy uncertainties remain modest relative to the several orders-of-magnitude dynamic range of the observed distributions.

4.3. Thermal energy distributions

The slope of the high-energy tail of the thermal-energy distribution is a key diagnostic for coronal heating: it determines whether the cumulative energy budget is dominated by rare large events or by numerous small ones (Hudson 1991). As above, we used CCDFs throughout for their binning-independent robustness (Clauset et al. 2009).

Figure 5 shows thermal-energy CCDFs for the four volume models of Sect. 3.4. Slopes were estimated by maximum likelihood above an objectively determined $E_{\rm min}$, with bootstrap confidence intervals obtained from 1000 resamplings. The inferred slopes cluster around $\alpha \approx 2.2$ for $A_{\rm proj}^{3/2}$-scaled models, with the Aschwanden model yielding a slightly steeper value reflecting its different geometry and the reduced chromospheric cutoff $h_{\rm ch} = 150$ km adopted here. The slopes span a range of $\alpha \approx 2.0$–2.4, reflecting differences in the adopted geometry; the scale-free character of the energy distribution is robust to geometric assumptions.

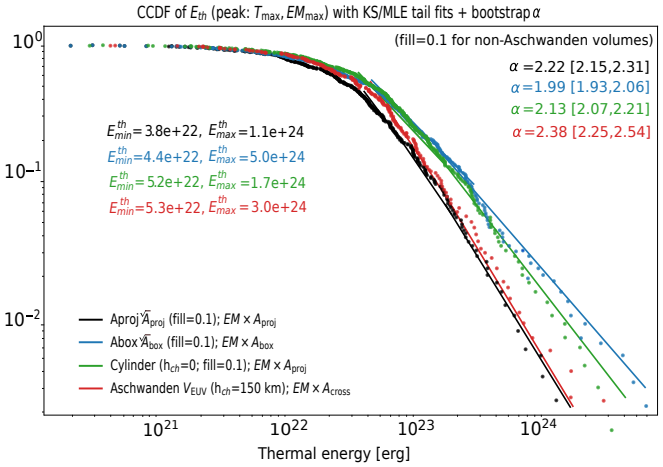

Fig. 5. CCDFs of campfire thermal energy ($E_{\rm th}$) for four geometric volume models: projected area ($A_{\rm proj}$; black), bounding-box area ($A_{\rm box}$; blue), cylindrical geometry (green), and Aschwanden-type EUV loop volume (red). A filling factor of 0.1 is applied for all non-Aschwanden volumes. Power-law fits are overplotted on the data above the KS-determined cutoff, $E_{\rm min}$; bootstrap 16th–84th percentile confidence intervals on α are quoted. The fitted energy range $[E_{\rm min}, E_{\rm max}]$ is indicated for each model. Slopes $\alpha \approx 2.0$–2.4 are consistent across all models, demonstrating robustness to geometric assumptions.

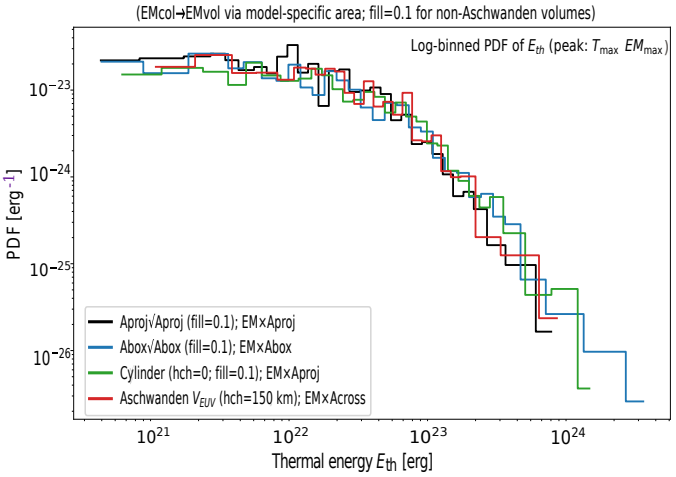

Fig. 6. Log-binned PDFs of campfire thermal energies for four volume models: $A_{\rm proj}$ (black), $A_{\rm box}$ (blue), cylindrical (green), and Aschwanden-type EUV loop (red). A filling factor of 0.1 is applied for all non-Aschwanden volumes. PDFs are shown for visual comparison; quantitative slope estimates are derived from the CCDFs (Fig. 5).

Complementary log-binned probability density functions (PDFs) are shown in Fig. 6 for comparison with earlier frequency-distribution studies. They were not used for slope estimation due to sensitivity to binning choices.

Campfire thermal energies extend to $\sim 5 \times 10^{24}$ erg and follow a power law with $\alpha > 2$. Events near this upper end are intrinsically rare, as reflected in the CCDF tails. This places campfires in the regime where small-scale events can in principle contribute significantly to coronal heating, if the power law extends below current detection limits.

Each campfire was assigned to a quiet-Sun atmospheric layer following the height stratification of Judge (2006). Figure 7 summarises the height dependence of key observables; Table 1 lists layer-resolved statistics. All quantities in this section were

Table 1. Campfire properties by atmospheric layer.

Layer	Height range (Mm)	N	Peak height (Mm)	$t_{\rm min}$ (s)	t_{90} (s)	t_{95} (s)	$V_{\rm max}$ (cm^3)	$E_{\rm th,16}$ (erg)	$E_{\rm th,84}$ (erg)
Photosphere	0.0–0.6	14	0.4	∼10	∼19	∼20	$\sim 9\times10^{21}$	$\sim 9\times10^{20}$	$\sim 7\times10^{21}$
Lower chromosphere	0.6–1.2	61	1.0	∼10	∼45	∼80	$\sim 4\times10^{23}$	$\sim 2\times10^{22}$	$\sim 10^{23}$
Upper chromosphere	1.2–1.5	62	1.4	∼10	∼39	∼45	$\sim 3\times10^{23}$	$\sim 2\times10^{22}$	$\sim 2\times10^{23}$
TR + low corona	1.5–2.0	214	1.8	∼10	∼35	∼40	$\sim 2\times10^{23}$	$\sim 10^{22}$	$\sim 2\times10^{23}$
Corona ($\beta < 1$)	2.0–2.4	217	2.2	∼10	∼35	∼55	$\sim 10^{23}$	$\sim 2\times10^{22}$	$\sim 2\times10^{23}$
Corona ($\beta \ll 1$)	>2.4	900	3.2	∼10	∼25	∼40	$\sim 4\times10^{23}$	$\sim 8\times10^{21}$	$\sim 10^{23}$

Notes. Atmospheric layers follow Judge (2006). Columns are: layer name; height range; number of events N; median peak height; minimum duration $t_{\rm min}$; the 90th and 95th percentiles of the duration distribution, t_{90} and t_{95}; the maximum emitting volume $V_{\rm max}$; and the 16th and 84th percentiles of the thermal energy, $E_{\rm th,16}$ and $E_{\rm th,84}$. Durations assume the 5 s HRI$_{\rm EUV}$ cadence; the shortest events may be single-frame detections ($t \lesssim 5$ s), with a two-frame minimum of $t_{\rm min} \approx 10$ s. The percentiles t_{90} and t_{95} characterise the typical upper duration while remaining insensitive to rare long-lived outliers; the full distribution tails are shown in Fig. 7b. Volumes and energies use background-subtracted DEM values with $EM_{\rm vol} = EM_{\rm col}A_{\rm proj}$ and $V_{\rm proj} = 0.1\,A_{\rm proj}\sqrt{A_{\rm proj}}$.

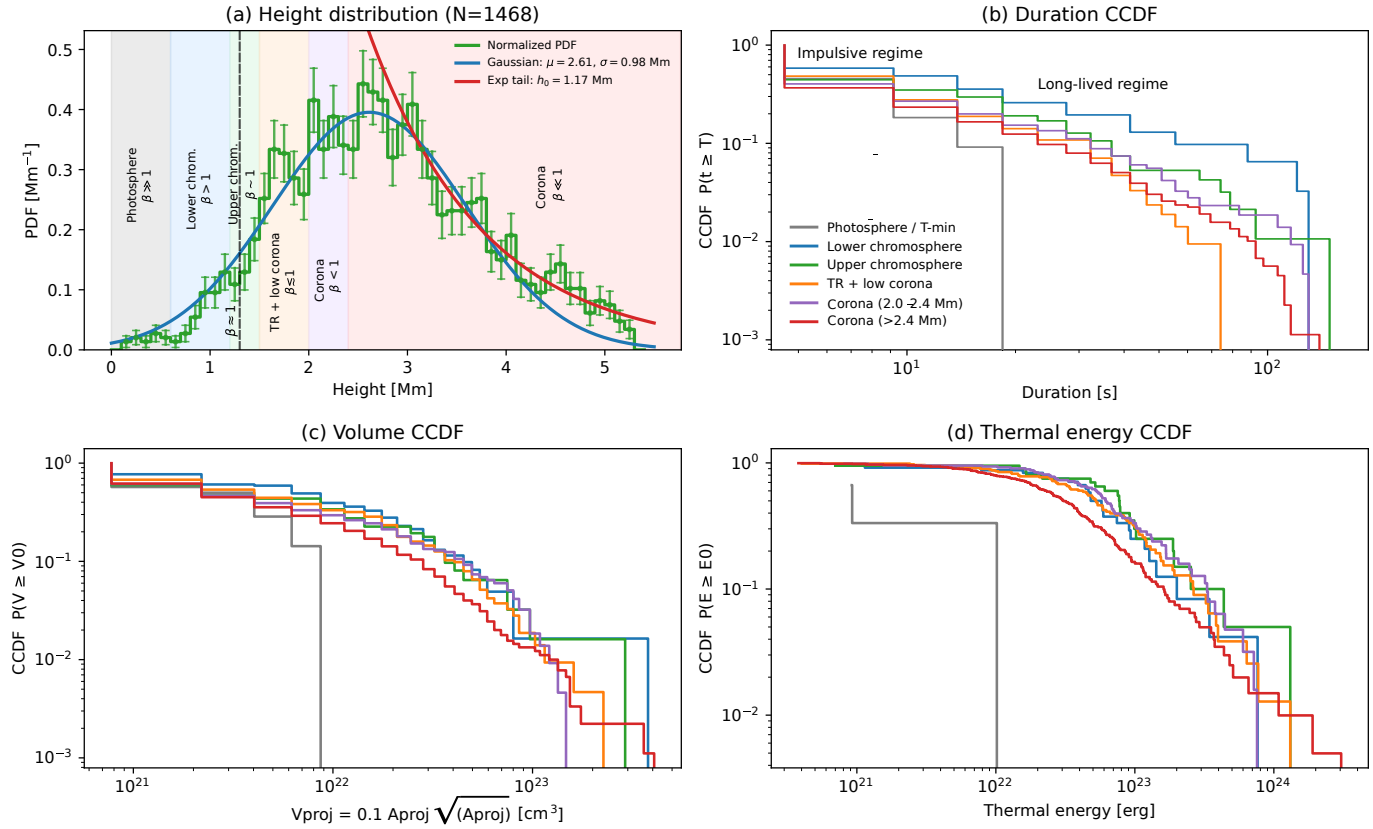

Fig. 7. Height dependence of campfire occurrence and properties following the quiet-Sun stratification of Judge (2006). *Panel (a)*: Height PDF with atmospheric layers and plasma-β regimes indicated. The core is well described by a Gaussian ($\mu = 2.61$ Mm, $\sigma = 0.98$ Mm); the high-altitude excess is fitted by an exponential tail ($h_0 = 1.17$ Mm). *Panel (b)*: Layer-resolved duration CCDFs (5 s cadence). Two regimes are visible: a short-duration impulsive regime common to all layers and a long-lived tail preferentially associated with chromospheric events. The tails extend to a few rare individual events of ∼150 s; the layer statistics in Table 1 use the 90th and 95th percentiles, which are insensitive to these outliers. *Panel (c)*: CCDFs of effective volume $V_{\rm proj} = 0.1\,A_{\rm proj}\sqrt{A_{\rm proj}}$. *Panel (d)*: CCDFs of background-subtracted thermal energy. Unlike duration, volume and thermal-energy distributions are broadly similar across layers, indicating that height-dependent plasma conditions modulate dissipation timescales rather than the energy scale of impulsive heating.

derived using background-subtracted DEM diagnostics and the baseline model $V_{\rm proj} = 0.1\,A_{\rm proj}\sqrt{A_{\rm proj}}$.

The height distribution (Fig. 7a) peaks in the corona, around ∼2.6 Mm (Gaussian centre $\mu = 2.61$ Mm), and extends both downwards to chromospheric layers and upwards to greater coronal heights. The core follows a Gaussian; a high-altitude tail indicates that campfires span plasma-β environments from $\beta \gtrsim 1$ at low heights to $\beta \ll 1$ in the corona.

The clearest height dependence is in event duration (Fig. 7b). Short-duration events occur at all heights with comparable probability; the shortest detectable duration is set by the cadence ($t \lesssim 5$ s single frame, $t_{\rm min} \approx 10$ s for two frames). Beyond this

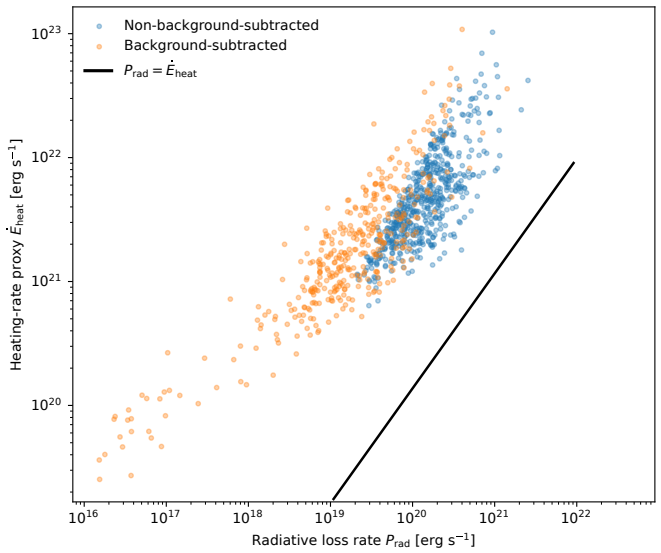

Fig. 8. Heating-rate proxy $\dot{E}_{heat} = E_{th}/t$ versus radiative loss rate $P_{rad} = EM_{vol}\,\Lambda(T)$, where $EM_{vol} = EM_{col}\,A_{proj}$ and $\Lambda(T)$ is the optically thin radiative loss function. Blue and orange circles show non-background-subtracted and background-subtracted DEM values, restricted to events with robust thermodynamic solutions (Berghmans et al. 2021). The diagonal line marks $P_{rad} = \dot{E}_{heat}$. All events lie well above this line, indicating that radiative losses alone cannot balance the injected thermal energy; non-radiative losses – primarily thermal conduction and enthalpy flux – must therefore play an important role in the energy budget.

floor, the lower chromosphere shows a clear excess of long-lived events extending to ∼80 s (∼9% of events there exceed 50 s, versus ∼3% at greater heights), while coronal events are predominantly short-lived (Table 1). A rank correlation across all individual events, independent of any layer binning, confirms this trend at high significance (Spearman $\rho = -0.11$, $p \approx 2 \times 10^{-5}$): although modest in amplitude, the anti-correlation between height and duration is statistically robust and driven primarily by the chromospheric excess of long-lived events.

By contrast, emitting volumes and thermal energies show only weak height dependence: as seen in Fig. 7c,d, the layer-resolved CCDFs overlap closely and span comparable ranges, in contrast to the clear layer-to-layer separation seen for the duration distributions (Fig. 7b). The primary layer-to-layer variation is in event lifetime, not energy scale (Table 1).

These results indicate that height-dependent plasma conditions primarily modulate the timescales of campfire evolution. The presence of long-duration events at chromospheric heights, without a corresponding shift in volume or energy, suggests that comparable energy is released over similar spatial scales but dissipated more slowly in denser, higher-β layers.

4.4. Heating rates and radiative losses

To assess the energetic consistency of campfire detections, we compared a heating-rate proxy with the radiative loss rate for each event. We computed

$$EM_{vol} = EM_{col}\,A_{proj}, \tag{1}$$

$$P_{rad} = EM_{vol}\,\Lambda(T), \tag{2}$$

where $\Lambda(T)$ is the optically thin radiative loss function at the DEM-derived temperature, and defined the heating-rate proxy as

$$\dot{E}_{heat} \equiv \frac{E_{th}}{t}, \tag{3}$$

with t the event duration. As shown in Fig. 8, $\dot{E}_{heat} \gg P_{rad}$ for all events, confirming that radiative losses represent a negligible correction to the heating-rate estimate and that non-radiative cooling channels – thermal conduction and enthalpy flux – dominate the energy budget.

We estimated the total campfire contribution to quiet-Sun coronal heating by summing the event thermal energies and normalising by the observing time and field-of-view area:

$$F_{heat} = \frac{\sum_i E_{th,i}}{A_{FOV}\,t_{obs}} \quad [\mathrm{erg\,cm^{-2}\,s^{-1}}]. \tag{4}$$

We obtain $F_{heat} \sim 10^2$–$10^{2.5}$ erg cm^{-2} s^{-1}, a sub-percent fraction of the canonical quiet-Sun loss rate of 3×10^5 erg cm^{-2} s^{-1} (Withbroe & Noyes 1977). This is a conservative lower limit: combining a lower 3σ detection threshold with the ∼26% DEM completeness (389 of the 1,468 events with robust background-subtracted DEM solutions) could raise the inferred contribution to a value of order a few percent of the canonical requirement (an approximate, single-epoch estimate in which the two corrections were treated as independent).

This result is consistent with earlier quiet-Sun studies. Ulyanov et al. (2019) find that directly detected events fall short of the required radiative losses by a factor of ∼30 and argue that the distribution must extend to lower energies to become sufficient. Krucker & Benz (1998) reported that microflares account for ∼16% of the quiet-corona output – a higher fraction than ours, most likely reflecting their larger event energies and the different methodology – their energies were derived from a two-filter line-ratio temperature estimate rather than the multi-channel DEM diagnostics used here. Similarly, Purkhart & Veronig (2022) find that SDO/AIA nanoflare-like events contribute ∼10% of the quiet-Sun radiative losses. The lower fraction found for campfires reflects our more stringent detection threshold and shorter observing window rather than an intrinsically smaller energy contribution; with $\alpha > 2$, the energy budget is expected to be dominated by the smallest, currently undetected events.

A key theoretical result from Hudson (1991) is that for $dN/dE \propto E^{-\alpha}$ with $\alpha > 2$, the total energy is dominated by the smallest events. With $\alpha \approx 2.2$, campfires could provide a pathway to coronal heating if the power law continues below current detection limits. We caution, however, that the observed distribution flattens below the fitted range, most likely owing to detection incompleteness rather than an intrinsic change in slope; whether the true slope remains above 2 in this regime cannot be established from the present data and must be tested by more sensitive future observations. The sub-percent flux is therefore a lower bound; smaller, unresolved events could supply the missing energy. This is consistent with – and does not contradict – studies showing that individual campfires contain sufficient local magnetic energy to power themselves (e.g. Panesar et al. 2021), which address the available energy reservoir rather than the area-averaged thermal-energy flux.

4.5. Comparison with previous studies

Figure 9 places campfires in the broader flare energy hierarchy, following the composite frequency distribution of Aschwanden

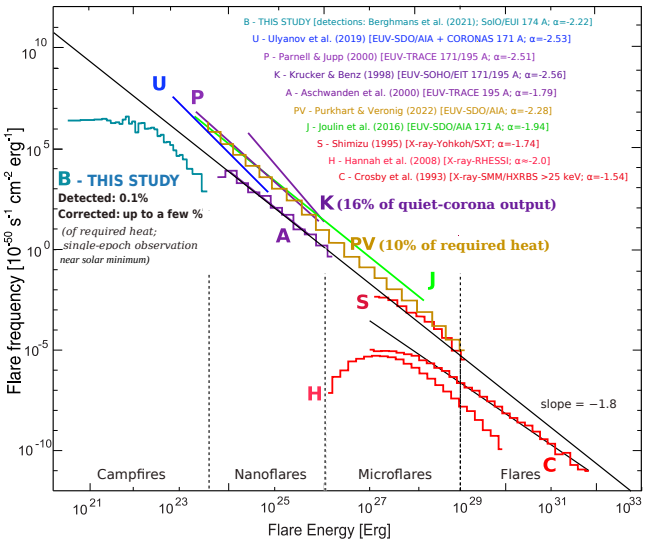

Fig. 9. Flare frequency distributions of campfire thermal energies compared with EUV, soft X-ray (SXR), and hard X-ray (HXR) flare populations, following Aschwanden et al. (2000). The distribution is normalised per unit time, area, and energy, allowing direct comparisons across event classes. Campfires occupy the low-energy end of the flare hierarchy with power-law slopes $\alpha = 1.99$–2.38 depending on the volume model; the reference $A_{\rm proj}^{3/2}$-scaled model gives $\alpha \approx 2.2$. The black diagonal line shows the reference slope of -1.8 from Aschwanden et al. (2000). Power-law indices for previous studies are taken from the literature. Curve B (this study) is based on the campfire detections of Berghmans et al. (2021), with thermal energies and the resulting frequency distribution derived here. It lies below the EUV/X-ray studies because of our stringent $\geq 5\sigma$ detection threshold; a lower threshold would shift it upwards. The heating-fraction percentages for the other studies are their published values, shown for comparison.

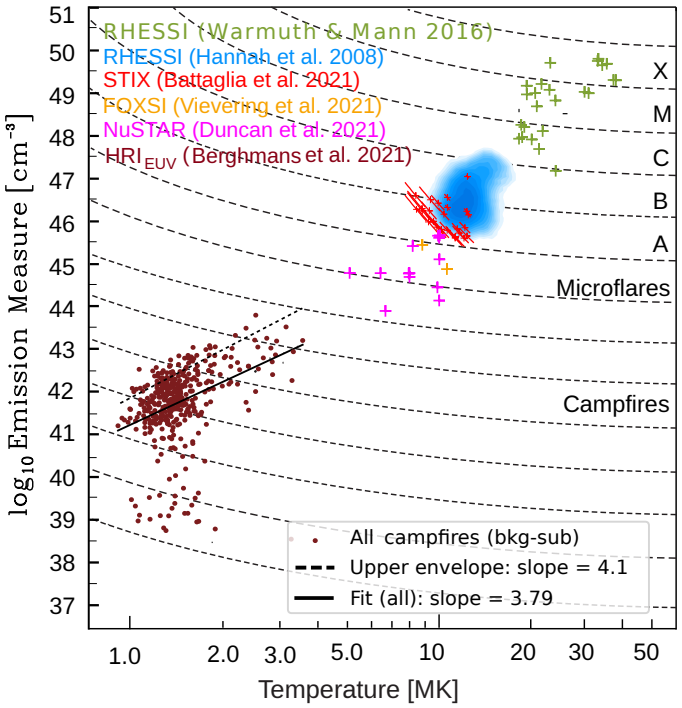

Fig. 10. EM–T diagram comparing EUI/HRI$_{\rm EUV}$ campfires (dark red circles; background-subtracted $EM_{\rm vol} = EM_{\rm col}\,A_{\rm proj}$) with larger solar flares from RHESSI (Hannah et al. 2008; Warmuth & Mann 2016), FOXSI (Vievering et al. 2021), *NuSTAR* (Duncan et al. 2021), and Solar Orbiter/STIX (Battaglia et al. 2021). The blue density map shows the RHESSI microflare population (Hannah et al. 2008). Campfire EM and T were first reported by Berghmans et al. (2021); here we re-analysed the same events with background subtraction. Both campfire fits use the background-subtracted data: the solid line shows a power-law fit to all campfire events ($EM_{\rm vol} \propto T^{3.79}$), while the straight dashed line shows the fit to their upper envelope (slope = 4.1), consistent with the $EM \propto T^4$ scaling of larger flares (Warmuth & Mann 2016). The faint curved dashed lines spanning the diagram mark contours of constant GOES soft X-ray flux, with the corresponding GOES classes indicated on the right axis. Campfires extend the EM–T continuum towards the lowest energies, connecting smoothly to the microflare population. This figure extends the EM–T comparison of Battaglia et al. (2021) to include EUI campfires at the low-energy end.

et al. (2000). Campfires occupy the low-energy extension of the flare distribution with power-law slopes $\alpha = 1.99$–2.38 depending on the volume model, consistent with the steep slopes required for small events to dominate the total energy budget (Hudson 1991). Notably, campfires extend to energies below the lower limit of previous quiet-Sun nanoflare studies, probing the impulsive-heating population at the smallest scales yet observed.

Prior EUV and X-ray studies using the Solar and Heliospheric Observatory (SOHO), the Transition Region and Coronal Explorer (TRACE), CORONAS-F, SDO, Yohkoh, and the Reuven Ramaty High Energy Solar Spectroscopic Imager (RHESSI) identified nanoflares and microflares with thermal energies spanning $\sim 10^{23}$–10^{26} erg, depending on temperature coverage, background treatment, and geometric assumptions (Crosby et al. 1993; Shimizu 1995; Krucker et al. 1997; Benz & Krucker 1998; Parnell & Jupp 2000; Hannah et al. 2008). The campfires analysed here populate the low-energy extension of this hierarchy, with background-subtracted thermal energies spanning $\sim 10^{20}$–10^{24} erg. The statistically robust power-law regime extends over one to two decades depending on the volume model: from $\sim 10^{22}$ erg for $A_{\rm proj}^{3/2}$-scaled models to $\sim 10^{23}$ erg for the Aschwanden model, up to $\sim 5 \times 10^{24}$ erg in all cases. Non-background-subtracted distributions shift upwards by ∼one order of magnitude, consistent with expectations for line-of-sight integrated EUV emission.

We note that below the fitted regime, in the range $\sim 10^{20}$–4×10^{22} erg, the distribution becomes flatter than the power-law tail. This flattening at the low-energy end is most likely caused by incomplete detection – a combination of the $\geq 5\sigma$ detection threshold, the limited sensitivity of HRI$_{\rm EUV}$, and the finite spatial resolution, which together cause the faintest and smallest events to be missed. We therefore fitted the power law only above $E_{\rm min}$, where the data are statistically robust, and did not treat the flat low-energy part as a real feature. As a result, our estimate of the campfire energy contribution is conservative: if the true distribution continues with $\alpha > 2$ below the completeness limit, the energy in smaller events would exceed what the observed flattening suggests. Probing this regime directly will require observations at closer perihelia, where the improved resolution and sensitivity of Solar Orbiter/EUI can push the completeness limit to lower energies. This energy range is supported by 3D MHD simulations: Chen et al. (2021) report thermal energies of 10^{22}–10^{24} erg for simulated campfire-like events, providing an important cross-validation of both the observational estimates and the adopted thermodynamic and geometric assumptions.

Figure 10 places campfires in the EM–T context of Solar Orbiter/STIX microflares. For the background-subtracted campfire data, the fit to all events ($EM_{\rm vol} \propto T^{3.79}$) and the upper-envelope fit (slope = 4.1) are consistent both with the

background-subtracted upper-envelope scaling derived independently in Fig. 2 (slope = 4.1) and with relations reported for larger flares (Warmuth & Mann 2016). Although STIX microflares probe significantly hotter plasma, their EM–T scaling follows the same qualitative trends as campfires, shifted towards higher temperatures and emission measures, indicating a common thermodynamic origin. Campfires thus extend the EM–T continuum of impulsive energy release from microflares down to picoflare energies, bridging the two populations without a discernible gap. Together with the layer-resolved analysis, this supports the view that campfires, nanoflares, and microflares form a continuous hierarchy distinguished by their atmospheric environment and cooling timescales – where event duration serves as a proxy for the EUV cooling time – rather than by fundamentally different energy-release mechanisms.

Following Ulyanov et al. (2019), we estimated how far below the detection limit the power law would need to extend for the integrated event energy to match the canonical heating flux of 3×10^5 erg cm^{-2} s^{-1} (Withbroe & Noyes 1977). Integrating the power-law distribution down to a lower energy $E_{\rm low}$ and equating the result to the required flux yields $E_{\rm low} \approx 2.4 \times 10^{17}$ erg for $\alpha = 2.2$, rising to $\approx 10^{21}$ erg for $\alpha = 2.5$. This strong sensitivity to α reflects the steepness of the energy integral: steeper slopes accumulate the required energy over a narrower range and therefore need not extend to such low energies.

Katsukawa & Tsuneta (2001) provide a useful order-of-magnitude benchmark: meeting the heating requirement with 10^{20} erg nanoflares demands 10^6 s^{-1} in a single active region – roughly six orders of magnitude more frequently than our detected campfires. This gap reflects our more stringent $\geq 5\sigma$ threshold; at 3σ the inferred contribution already reaches ∼1.2%. Accounting further for the ∼26% DEM completeness could add a further factor of a few, bringing the total to a value of order a few percent overall. Additionally, our energies capture only the coronal (∼1 MK) component; campfire plasma also emits in cooler transition-region lines (Dolliou et al. 2023, 2024; Huang et al. 2023), so the true energy budget extends beyond EUV imaging alone. Coordinated EUI and SPICE observations are uniquely placed to constrain the full campfire energy budget (Narang et al. 2025). As a remote-sensing estimate from a single epoch, the precise fraction cannot be pinned down definitively; it depends on the observing region, the phase of the solar cycle, and the detection limits. We therefore present it as a robust order-of-magnitude result rather than a final figure. Its significance lies less in the exact percentage than in the fact that an impulsive-heating population is now detectable down to picoflare energies and is beginning to be resolved by atmospheric layer.

4.6. Limitations of our analysis

The thermal energies represent only the excess thermal component from EUV emission, not the total available magnetic energy. Other energy channels – bulk motions, waves, non-thermal particles (Warmuth & Mann 2020) – are not constrained here, so the inferred values are lower limits to the total energy released.

Our sample may also be incomplete in terms of temperature. The $\mathrm{HRI_{EUV}}$ 174 Å passband responds mainly to plasma near ∼1 MK, so events that heat plasma predominantly to higher or lower temperatures would emit weakly in this channel and could escape detection entirely. Such events would be absent from our catalogue rather than merely underestimated in energy, so the detected population, and hence the inferred heating contribution, represents a lower limit also in this respect.

The dominant systematic uncertainty is the emitting volume, which cannot be measured directly. The four geometric models explored here span the range commonly used in the field; their consistency demonstrates that the main statistical conclusions are robust to geometric assumptions.

Temperatures and emission measures come from the DEM analysis of Paper I (Berghmans et al. 2021), performed using the regularised inversion method of Hannah & Kontar (2012). Different DEM inversion methods can yield somewhat different temperature estimates (Hofmeister et al. 2025); the uncertainties in Paper I reflect internal consistency rather than the full systematic range. Since

$$E_{\rm th} \propto T\ \sqrt{\mathrm{EM_{vol}}\, V},$$

fractional emission-measure uncertainties propagate as half their value into $E_{\rm th}$, while fractional temperature uncertainties propagate directly. Emission measure is therefore the dominant source of error for individual events, though population-level distributions – shape, slope, dynamic range – are unaffected.

Finally, these results derive from a single 245 s sequence near solar minimum, ensuring a clean quiet-Sun sample but limiting generalisability to other activity levels or magnetic environments. Future multi-epoch observations will be needed to assess how campfire properties vary with solar cycle phase.

5. Discussion

Individual current sheets do not dissipate in isolation (Vlahos 1994); the observed EUV response reflects the collective thermal effect of many unresolved dissipation sites distributed along the magnetic structure. This picture is supported by 3D MHD simulations that reproduce campfire EUV brightenings as the plasma response to localised current dissipation, without resolving the underlying kinetic-scale sheets (Chen et al. 2021). EUV campfires therefore constrain the macroscopic plasma response – spatial extent, characteristic timescales, and thermal signatures – rather than the dissipation process itself.

The height dependence of event duration (Fig. 7) – driven by the excess of long-lived events in the lower chromosphere – without an analogous dependence in energy or volume, provides a clear observational anchor for height-dependent dissipation and cooling regimes. Perpendicular current sheets dissipating via magnetic reconnection are expected to reach kinetic scales of tens to hundreds of metres. By contrast, in the low corona where $\beta \sim 1$, quasi-parallel current sheets are predicted to be systematically wider – by roughly an order of magnitude – owing to lower dissipation thresholds and reduced magnetic shear (Demoulin & Klein 2000). Such broader structures favour gentler, thermally dominated energy release on sound-speed-limited timescales of tens to hundreds of seconds, consistent with the observed excess of long-duration campfires at chromospheric heights (e.g. Pontin et al. 2017). The observed duration distribution, spanning both rapid (∼10 s) and gradual (∼100 s) events, may thus reflect a transition from fast Alfvénic dissipation in low-β coronal plasma to slower, thermally dominated dissipation in higher-β plasma near the transition region. The absence of a height dependence in thermal energy indicates that comparable amounts of magnetic energy are released over similar spatial scales but on different timescales, consistent with both perpendicular reconnection and parallel current dissipation operating in the low corona (Klimchuk 2015, 2017). Taken together, these results reinforce the view that EUV observations capture thermodynamic envelopes of unresolved, intermittent magnetic energy dissipation – precisely as anticipated by modern coronal-heating theory.

6. Conclusions

We have presented a thermal-energy analysis of EUV campfires observed in the quiet Sun by Solar Orbiter/EUI HRI_{EUV} and catalogued by Berghmans et al. (2021), building on the thermodynamic diagnostics of Paper I. We quantified thermal energies, heating-rate proxies, and statistical distributions using multiple geometric volume models, and compared the campfire population with Solar Orbiter/STIX microflares (Battaglia et al. 2021), SDO/AIA nanoflare-like events (Purkhart & Veronig 2022), and earlier flare statistics. Our main conclusions are:

1. Campfires occupy the picoflare energy regime, with background-subtracted thermal energies spanning $\sim 10^{20}$–10^{24} erg and rare events reaching $\sim 5 \times 10^{24}$ erg. Their high-energy tails follow power-law behaviour over ∼1.5–2 decades with slopes $\alpha \approx 2.0$–2.4 depending on the adopted volume model; the reference $A_{\rm proj}^{3/2}$-scaled model gives $\alpha \approx 2.2$, consistent with a low-energy extension of the solar flare hierarchy.
2. The EM–T scaling of campfires ($EM_{\rm vol} \propto T^{3.79}$, upper-envelope slope = 4.1) is consistent with relations reported for larger flares (Warmuth & Mann 2016), supporting their interpretation as the low-energy extension of impulsive heating in magnetically confined plasma and connecting smoothly to the microflare population without a discernible gap.
3. The statistical properties – energy range, distribution shape, and power-law slope – are robust against reasonable variations in source geometry, background subtraction, and instrumental uncertainties, indicating that the observed scaling is intrinsic to the campfire population.
4. Campfires span atmospheric heights from the chromosphere into the corona, with the occurrence distribution peaking around ∼2.6 Mm, covering plasma-β regimes from $\beta \gtrsim 1$ to $\beta \ll 1$, with no evidence of discrete sub-populations.
5. Campfire durations exhibit a clear height dependence: short events occur at all heights, but the lower chromosphere shows an enhanced fraction of long-lived brightenings (∼9% exceed 50 s, versus ∼3% at greater heights). Emitting volumes and thermal energies, by contrast, are broadly similar across layers (with at most a slight decrease in the high corona). This indicates that height-dependent plasma conditions modulate dissipation and cooling timescales rather than the characteristic energy scale – consistent with slower current dissipation in higher-β plasma near the transition region.
6. Heating-rate proxies exceed radiative loss rates at all heights, confirming that campfires are heating-dominated impulsive events. Directly detected campfires contribute ∼0.1% of the canonical quiet-Sun heating requirement (Withbroe & Noyes 1977). This is a conservative lower limit: lowering the detection threshold to 3σ and accounting for the ∼26% DEM completeness could together raise the contribution to a value of order a few percent (up to ∼5%) of the canonical requirement. This combined factor is an order-of-magnitude estimate: the two corrections were treated as independent, and the underlying Poisson and threshold uncertainties were not propagated in detail. With $\alpha > 2$ (Hudson 1991), the energy integral is dominated by the smallest events; if the power law extends with the same slope below our detection limit, unresolved events could supply a significant additional fraction. Whether the slope remains this steep in the incompletely sampled low-energy range remains to be established by more sensitive observations. Coordinated EUI and SPICE observations, combined with lower detection thresholds, are therefore the most direct path towards a complete census of the campfire energy budget.
7. These results are based on a single observing sequence near solar minimum, providing a clean quiet-Sun sample. Multi-epoch observations across the solar cycle will be needed to establish whether the height-resolved trends reported here are universal.

The overarching finding of this work is that EUV campfires extend the impulsive-heating population to the lowest energies yet probed in the quiet Sun, although their full energetic role remains to be quantified. The directly detected population accounts for a measurable fraction of the heating requirement (∼0.1%). Accounting approximately for the detection threshold and DEM completeness raises this estimate to a value of order a few percent, though we stress that this is a single-epoch, order-of-magnitude estimate without full uncertainty propagation. Whether the contribution increases further at still lower energies cannot be determined from the present data; the steep power-law slope ($\alpha > 2$) means this remains an open possibility, to be tested by future observations reaching below our current detection limit.

It is important to distinguish two complementary aspects of the campfire energy budget. Studies of individual campfires have shown that their available magnetic energy is sufficient to power the local brightening (Panesar et al. 2021) – establishing that the energy source exists at the level of individual events. The present work addresses a different and harder question: whether the integrated thermal output of the campfire population, summed over the field of view and normalised to the quiet-Sun area, can account for the global coronal heating requirement. Our results show that the detected population falls short. The associated uncertainties are large enough that we cannot rule out a substantial contribution from events below the current $\geq 5\sigma$ detection threshold: with $\alpha > 2$, such unresolved events could in principle supply a significant additional fraction of the heating requirement. Two conditions must be simultaneously satisfied for campfire-like events to dominate coronal heating (Hudson 1991; Katsukawa & Tsuneta 2001): the energy distribution must follow a power law with $\alpha > 2$, so that the energy integral diverges towards smaller events; and the occurrence rate of small events must be sufficiently high. Our measured slope of $\alpha \approx 2.2$ satisfies the first condition. The second remains to be tested observationally at energies below our current detection threshold – precisely the regime accessible to future Solar Orbiter campaigns at closer perihelia and with coordinated SPICE spectroscopy.

The key physical insight from the layer-resolved analysis is that atmospheric stratification primarily regulates dissipation and thermal relaxation timescales rather than the energy scale of impulsive heating. This provides a new observational constraint distinguishing between current-dissipation models operating in different plasma-β regimes. Future coordinated observations with Solar Orbiter EUI and SPICE, at progressively closer perihelia and with lower detection thresholds, offer the most direct route to resolving whether the campfire population – and the broader class of small-scale EUV brightenings – can account

for a dominant fraction of the energy required to maintain the quiet-Sun corona.

Code availability

A Python implementation of the methods for calculating campfire volumes, emission measures, and thermal energies is available at `https://github.com/epodlad/campfire-thermal-energy`. The repository was released after journal publication and documents the formulas, assumptions, input requirements, and validation status.

Acknowledgements. We thank the anonymous referee for constructive comments that helped clarify the interpretation of the results and motivated a more coherent synthesis of impulsive heating, current dissipation, and plasma processes in the low solar corona. The Solar Orbiter mission is a space mission of international collaboration between ESA and NASA, operated by ESA. The EUI instrument was built by a consortium led by CSL, including IAS, MPS, MSSL/UCL, PMOD/WRC, ROB, and LCF/IO, with funding from the Belgian Federal Science Policy Office (BELSPO/PRODEX PEA 4000134088, 4000112292, and 4000106864); the Centre National d'Etudes Spatiales (CNES); the UK Space Agency (UKSA); the Bundesministerium für Wirtschaft und Energie (BMWi) through the Deutsches Zentrum für Luft- und Raumfahrt (DLR); and the Swiss Space Office (SSO). The ROB team thanks BELSPO for support through the ESA-PRODEX programme (grants 4000134088, 4000112292, 4000136424, and 4000134474). D.M.L. is grateful to the UK Science and Technology Facilities Council (STFC) for an Ernest Rutherford Fellowship (ST/R003246/1). P.A. acknowledges funding from an STFC Ernest Rutherford Fellowship (ST/R004285/2). O.P. is grateful to the German Leibniz Association and the MWFK Brandenburg. The work of F.S. was supported by DLR grant 50 OT 1904. A.M.V. and S.P. acknowledge the Austrian Science Fund (FWF): project 10.55776/I4555-N.

References

Aschwanden, M. J. 2004, Physics of the Solar Corona. An Introduction (Praxis Publishing Ltd.)
Aschwanden, M. J., Tarbell, T. D., Nightingale, R. W., et al. 2000, ApJ, 535, 1047
Bak, P., Tang, C., & Wiesenfeld, K. 1987, Phys. Rev. Lett., 59, 381
Battaglia, A. F., Saqri, J., Massa, P., et al. 2021, A&A, 656, A4
Benz, A. & Krucker, S. 1998, Sol. Phys., 182, 349
Benz, A. O. 2008, Living Rev. Sol. Phys., 5, 1
Berghmans, D., Auchère, F., Long, D., et al. 2021, A&A, 656, L4
Bertalmío, M., Bertozzi, A. L., & Sapiro, G. 2001, in Proceedings of the 2001 IEEE Computer Society Conference on Computer Vision and Pattern Recognition (CVPR 2001), Vol. 1 (Kauai, HI, USA: IEEE Computer Society), I–355–I–362
Chen, Y., Przybylski, D., Peter, H., et al. 2021, A&A, 656, L7
Chitta, L. P., Huang, Z., D'Amicis, R., et al. 2025, A&A, 694, A71
Chitta, L. P., Peter, H., & Young, P. R. 2021, A&A, 647, A159
Chitta, L. P., Zhukov, A. N., Berghmans, D., et al. 2023, Science, 381, 867
Clauset, A., Shalizi, C. R., & Newman, M. E. J. 2009, SIAM Rev., 51, 661
Cranmer, S. R., Gibson, S. E., & Riley, P. 2017, Space Sci. Rev., 212, 1345
Crosby, N. B., Aschwanden, M. J., & Dennis, B. R. 1993, Sol. Phys., 143, 275
De Moortel, I. & Browning, P. 2015, Philos. Trans. R. Soc. A, 373, 20140269
Demoulin, P. & Klein, K.-L. 2000, in Transport and Energy Conversion in the Heliosphere, ed. J. P. Rozelot, L. Klein, & J. C. Vial, Vol. 553, 99
Dolliou, A., Parenti, S., Auchère, F., et al. 2023, A&A, 671, A64
Dolliou, A., Parenti, S., & Bocchialini, K. 2024, A&A, 688, A77
Duncan, J., Glesener, L., Grefenstette, B. W., et al. 2021, ApJ, 908, 29
Georgoulis, M. K., Velli, M., & Einaudi, G. 1998, ApJ, 497, 957
Georgoulis, M. K. & Vlahos, L. 1996, ApJ, 469, L135
Guerreiro, N., Haberreiter, M., Hansteen, V., & Schmutz, W. 2017, A&A, 603, A103
Hahn, M., Hofmeister, S. J., Koukras, A., & Savin, D. W. 2025, ApJ, 991, 97
Hahn, M. & Savin, D. W. 2014, ApJ, 795, 111
Hannah, I. G., Christe, S., Krucker, S., et al. 2008, ApJ, 677, 704
Hannah, I. G. & Kontar, E. P. 2012, A&A, 539, A146
Heyvaerts, J. & Priest, E. R. 1983, A&A, 117, 220
Hofmeister, S. J., Asvestari, E., Dissauer, K., et al. 2025, arXiv preprint arXiv:2509.04663 [arXiv:2509.04663]
Huang, Z., Teriaca, L., Aznar Cuadrado, R., et al. 2023, A&A, 673, A82
Hudson, H. S. 1991, Sol. Phys., 133, 357
Joulin, V., Buchlin, E., Solomon, J., & Guennou, C. 2016, A&A, 591, A148
Judge, P. G. 2006, in ASP Conference Series, Vol. 354, 259–272
Katsukawa, Y. & Tsuneta, S. 2001, ApJ, 557, 343
Klimchuk, J. A. 2015, Philos. Trans. R. Soc. A, 373, 20140256
Klimchuk, J. A. 2017, arXiv e-prints, arXiv:1709.07320
Krucker, S., Benz, A., Bastian, T., & Acton, L. 1997, in Proceedings of the SOHO Workshop
Krucker, S. & Benz, A. O. 1998, ApJ, 501, L213
Lemen, J. R., Title, A. M., Akin, D. J., et al. 2012, Sol. Phys., 275, 17
Leontovich, M. A. 1975, Sov. J. Plasma Phys., 1, 395
Müller, D., St. Cyr, O. C., Zouganelis, I., et al. 2020, A&A, 642, A1
Narang, N., Verbeeck, C., Mierla, M., et al. 2025, A&A, 699, A138
Panesar, N. K. et al. 2021, A&A, 656, L3
Parenti, S., Del Zanna, G., Petralia, A., et al. 2017, ApJ, 846, 25
Parker, E. N. 1988, ApJ, 330, 474
Parnell, C. E. & Jupp, P. E. 2000, ApJ, 529, 554
Pesnell, W. D., Thompson, B. J., & Chamberlin, P. C. 2012, Sol. Phys., 275, 3
Pontin, D. I., Thurgood, J. O., & McLaughlin, J. A. 2017, Phys. Plasmas, 24, 062904
Priest, E. & Forbes, T. 2000, Magnetic reconnection: MHD theory and applications (Cambridge, Un. P.)
Purkhart, S. & Veronig, A. M. 2022, A&A, 661, A149
Rappazzo, A. F., Velli, M., Einaudi, G., & Dahlburg, R. B. 2008, ApJ, 677, 1348
Rochus, P., Auchère, F., Berghmans, D., et al. 2020, A&A, 642, A8
Shimizu, T. 1995, PASJ, 47, 251
Spicer, D. S. & Brown, J. C. 1980, Sol. Phys., 67, 385
Subramanian, S., Kashyap, V. L., Tripathi, D., Madjarska, M. S., & Doyle, J. G. 2018, A&A, 615, A47
Tomczyk, S., McIntosh, S. W., Keil, S. L., et al. 2007, Science, 317, 1192
Ulyanov, A. S., Bogachev, S. A., Reva, A. A., Kirichenko, A. S., & Loboda, I. P. 2019, Astron. Lett., 45, 248
Verbeeck, C., Kraaikamp, E., Ryan, D. F., & Podladchikova, O. 2019, ApJ, 884, 50
Vievering, J. T., Glesener, L., Panchapakesan, S. A., et al. 2021, ApJ, 913, 15
Vlahos, L. 1994, Space Sci. Rev., 68, 39
Vlahos, L., Georgoulis, M., Kluiving, R., & Paschos, P. 1995, A&A, 299, 897
Warmuth, A. & Mann, G. 2016, A&A, 588, A115
Warmuth, A. & Mann, G. 2020, A&A, 644, A172
Withbroe, G. L. & Noyes, R. W. 1977, ARA&A, 15, 363
Zhukov, A., Mierla, M., Auchère, F., et al. 2021, A&A, 656, A35

[1] Leibniz Institute for Astrophysics Potsdam, An der Sternwarte 16, 14482 Potsdam, Germany
[2] Physikalisch-Meteorologisches Observatorium Davos, World Radiation Center, 7260 Davos Dorf, Switzerland
[3] ETH-Zürich, Wolfgang-Pauli-Str. 27, 8093 Zürich, Switzerland
[4] Solar-Terrestrial Centre of Excellence – SIDC, Royal Observatory of Belgium, Ringlaan -3- Av. Circulaire, 1180 Brussels, Belgium
[5] Johns Hopkins University Applied Physics Laboratory, 11100 Johns Hopkins Rd, Laurel, MD 20723, USA
[6] Research Center for Astronomy and Applied Mathematics (RCAAM), Academy of Athens, 11527 Athens, Greece (on leave)
[7] University of Graz, Institute of Physics, Universitätsplatz 5, 8010 Graz, Austria
[8] University of Graz, Kanzelhöhe Observatory for Solar and Environmental Research, 9521 Treffen, Austria
[9] European Space Agency (ESA/ESTEC), 2200 AG Noordwijk, The Netherlands
[10] Columbia Astrophysics Laboratory, Columbia University, 550 West 120th Street, New York, NY 10027, USA
[11] School of Engineering, Physics and Mathematics, Northumbria University, Newcastle Upon Tyne, NE1 8ST, UK
[12] Centre for Astrophysics & Relativity, School of Physical Sciences, Dublin City University, Glasnevin Campus, Dublin, D09 V209, Ireland
[13] IRSOL, Istituto Ricerche Solari Aldo e Cele Daccò, Università della Svizzera italiana, 6605 Locarno Monti, Switzerland
[14] Institute of Geodynamics, Romanian Academy, 020032 Bucharest, Romania
[15] Université Paris-Saclay, CNRS, Institut d'Astrophysique Spatiale, 91405 Orsay, France
[16] Institute of Applied Computing & Community Code, Universitat de les Illes Balears, 07122 Palma de Mallorca, Spain
[17] European Space Agency (ESA/ESAC), E-28692 Villanueva de la Cañada, Madrid, Spain

[18] Centre Spatial de Liège, Université de Liège, 4031 Angleur, Belgium
[19] Max Planck Institute for Solar System Research, 37077 Göttingen, Germany
[20] UCL-Mullard Space Science Laboratory, Holmbury St. Mary, Dorking, Surrey RH5 6NT, UK